A&A 462, 657–666 (2007)
DOI: 10.1051/0004-6361:20065406

Astronomy & Astrophysics

XMM-Newton and INTEGRAL spectroscopy of the microquasar GRO J1655–40 during its 2005 outburst

M. Díaz Trigo[1], A. N. Parmar[1], J. Miller[2], E. Kuulkers[3], and M. D. Caballero-García[4]

[1] Astrophysics Mission Division, Research and Scientific Support Department of ESA, ESTEC, Postbus 299, 2200 AG Noordwijk, The Netherlands
e-mail: mdiaz@sciops.esa.int
[2] Department of Astronomy, University of Michigan, 500 Church Street, Dennison 814, Ann Arbor, MI 48109, USA
[3] Integral Science Operations Centre, Science Operations and Data Systems Division, Research and Scientific Support Department of ESA, ESAC, Apartado 50727, 28080 Madrid, Spain
[4] Laboratorio de Astrofísica Espacial y Física Fundamental, INTA, Apartado 50727, 28080 Madrid, Spain

Received 11 April 2006 / Accepted 20 October 2006

ABSTRACT

We report on two simultaneous XMM-Newton and INTEGRAL observations of the microquasar GRO J1655−40 during the 2005 outburst when the source was in its high-soft state. The 0.3–200 keV spectra are complex with an overall continuum which may be modeled using an absorbed blackbody together with a weak, steep, power-law component. In addition, there is evidence for the presence of *both* a relativistically broadened Fe K line and a highly photo-ionized absorber. The photo-ionized absorber is responsible for strong K absorption lines of Fe XXV and Fe XXVI in the EPIC pn spectra and blue-shifted ($v = -540 \pm 120$ km s^{-1}) Ne X and Fe XXIV features in the RGS spectra. The parameters of the photo-ionized absorber were different during the two observations with the ionization parameter, $\log(\xi)$, decreasing from 3.60 ± 0.04 to 3.30 ± 0.04 erg cm s^{-1} and the column density decreasing from $(5.2\pm1.0) \times 10^{22}$ atom cm^{-2} to $(1.5\pm1.0) \times 10^{22}$ atom cm^{-2} during the first and second observations as the 0.5–200 keV GRO J1655−40 luminosity decreased by around a half. At 90% confidence the INTEGRAL data show no evidence of a break in the power-law component up to energies of 380 keV and 90 keV for the first and second observations, respectively.

Key words. X-rays: binaries – accretion, accretion disks – X-rays: individuals: GRO J1655−40

1. Introduction

The X-ray nova GRO J1655−40 was discovered using the Burst and Transient Source Experiment (BATSE) onboard the Compton Gamma Ray Observatory (Zhang et al. 1994). Soon after the discovery radio observations revealed apparently superluminal relativistic jets moving in opposite directions almost perpendicular to the line of sight (85°) with a velocity of 0.92 c (Hjellming & Rupen 1995; Tingay et al. 1995). Optical observations, obtained when the system had returned to quiescence, showed that the companion star is a F3–5 giant or sub-giant in a 2.62 day orbit around a 5–8 $M_{\odot}$ compact object, which is almost certainly a black hole (Orosz & Bailyn 1997; Van der Hooft et al. 1998; Shahbaz et al. 1999). GRO J1655−40 has been observed to undergo deep absorption dips (Kuulkers et al. 1998; Balucińska-Church 2001; Tanaka et al. 2003; Kuulkers et al. 2000) consistent with observing the source at an inclination angle of ∼70° (Van der Hooft et al. 1998). This indicates that the inclination of the inner disk may differ slightly from the inclination of the binary system. This misalignment may arise if the jet axis coincides with the spin axis of the compact object and the inner disk is anchored perpendicular to this axis by gravitational and magneto-hydrodynamic effects. The misalignment of the binary plane and the jet could be explained by the Bardeen-Petterson effect (Maccarone 2002). GRO J1655−40 has been subject of a considerable number of studies using X-ray timing, presenting the highest-frequency quasi-periodic oscillations (QPOs) yet seen in a black hole (450 Hz, Strohmayer 2001).

Narrow X-ray absorption lines from highly ionized Fe were first detected from GRO J1655−40 (Ueda et al. 1998; Yamaoka et al. 2001) and from another superluminal jet source GRS 1915+105 (Kotani et al. 2000; Lee et al. 2002). Similar features were subsequently detected from the low-mass X-ray binary (LMXB) GX 13+1 (Ueda et al. 2001) and from all the bright dipping LMXBs observed with XMM-Newton (Díaz Trigo et al. 2006). The changes in the X-ray continuum and the Fe absorption features during dips are explained as resulting primarily from an increase in column density and a decrease in the ionization state of a highly-ionized absorber (Boirin et al. 2005; Díaz Trigo et al. 2006). Since dipping sources are simply normal LMXBs viewed from close to the orbital plane, this implies that ionized absorbers are a common feature of LMXBs. Outside of the dips, the properties of the absorption features do not vary strongly with orbital phase. This suggests that the ionized plasma in LMXBs has a cylindrical geometry with a maximum column density close to the plane of the accretion disk.

Recently *Chandra* HETGS observations of the black hole candidates GX 339−4, XTE J1650−500 and H 1743−322 (Miller et al. 2004, 2006b) have revealed the presence of variable, blue-shifted, highly-ionized absorption features which are interpreted as evidence for outflows. While Fe XXV and Fe XXVI features are present in the H 1743−322 spectrum, GX 339−4 and XTE J1650−500 show O VIII and Ne IX or Ne II features from less ionized material. These features suggest that a warm absorber analogous to those seen in many Seyfert galaxies

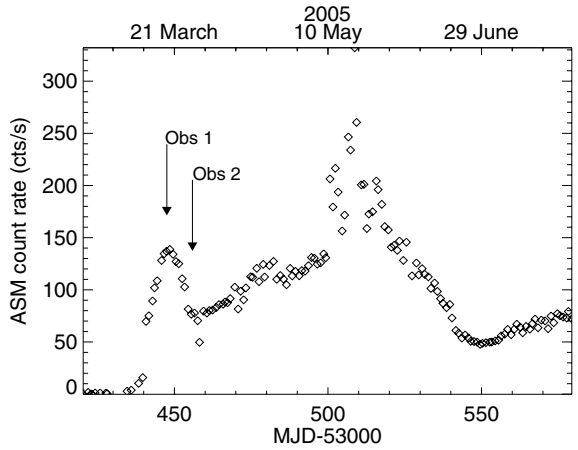

Fig. 1. ASM 1.5–12 keV lightcurve of GRO J1655−40. The times of the XMM-Newton and INTEGRAL observations reported here are indicated with arrows.

is present in systems such as GX 339−4 and XTE J1650−500 (Miller et al. 2004). In contrast, Miller et al. (2006b) propose that the absorber present in H 1743−322 is more highly ionized.

We report on two simultaneous XMM-Newton and INTEGRAL observations of GRO J1655−40 obtained during a recent outburst that started around 2005 February 17 (Markwardt & Swank 2005) and reached a maximum intensity of ∼5 Crab during flares around 2005 May 20. RXTE (Homan 2005) and *Swift* (Brocksopp et al. 2006) monitored the outburst and near-simultaneous observations to the XMM-Newton and INTEGRAL observations are available. Figure 1 shows the RXTE All-Sky Monitor (ASM) lightcurve of part of the 2005 outburst with the times of the XMM-Newton and INTEGRAL observations indicated.

2. Observations and data analysis

2.1. XMM-Newton observations

The XMM-Newton Observatory (Jansen et al. 2001) includes three 1500 cm^2 X-ray telescopes each with an European Photon Imaging Camera (EPIC, 0.1–15 keV) at the focus. Two of the EPIC imaging spectrometers use MOS CCDs (Turner et al. 2001) and one uses pn CCDs (Strüder et al. 2001). Reflection Grating Spectrometers (RGS, 0.35–2.5 keV, Den Herder et al. 2001) are located behind two of the telescopes. GRO J1655−40 was observed by XMM-Newton for 23.8 ks on 2005 March 18 between 15:47 and 22:25 UTC (Obs ID 0155762501, hereafter called Obs 1) and for 22.4 ks on 2005 March 27 between 08:43 and 14:56 UTC (Obs ID 0155762601, hereafter called Obs 2). The thin optical blocking filter was used with the EPIC camera. The EPIC pn camera was operated in burst mode due to the high count rate of the source (≳5000 s^{-1}). For the same reason, the EPIC MOS cameras were not operated. RGS2 was operated in its normal spectroscopy mode with all CCD chips read in parallel. However, the individual RGS1 CCD chips were read out sequentially. This reduces the frame time from 4.8 to 0.6 s (4.8/8) and consequently the pile-up by almost an order of magnitude. All the X-ray data products were obtained from the XMM-Newton public archive and reduced using the Science Analysis Software (SAS) version 6.1.0.

In pn burst mode, only one CCD chip (corresponding to a field of view of 13.′6 × 4.′4) is used and the data from that chip are collapsed into a one-dimensional row (4.′4) to be read out at high speed, the second dimension being replaced by timing information. The duty cycle is only 3%. This allows a time resolution of 7 μs, and photon pile-up occurs only for count rates above 60 000 s^{-1}. Only single and double events (patterns 0 to 4) were selected. Source events were extracted from a 53″ wide column centered on the source position (RAWX 30 to 43). Background events were obtained from a column of the same width, but centered 115″ from GRO J1655−40 (RAWX 2 to 15). Due to the brightness of the source, the region used to extract the background is highly contaminated by source events. For this reason we did not subtract the background from the source which is anyway negligible for such a strong source. Ancillary response files were generated using the SAS task `arfgen`. Response matrices were generated using the SAS task `rmfgen`. We used burst mode pn data in the 0.5–10 keV energy range.

The SAS task `rgsproc` was used to produce calibrated RGS event lists, spectra, and response matrices. The RGS2 spectra were strongly piled-up and could not be used reliably. Pile-up in the XMM-Newton gratings is rare, and we have been unable to find a method to correct for pile-up in the literature. For RGS1, less than 5% of events are affected by pile-up in all CCDs except number 8 covering the energy range 1.18–1.6 keV, where pile-up may have reached 25% during Obs 1 and 15% in Obs 2. This will strongly affect continuum measurements, but the derived properties of any narrow line features will not be so strongly affected. Therefore we only used RGS1 data from the first and second orders.

2.2. INTEGRAL observations

The INTEGRAL (Winkler et al. 2003) payload consists of two main gamma-ray instruments, one of which is optimized for 15 keV to 10 MeV high-resolution imaging (IBIS, Ubertini et al. 2003) and the other for 18 keV to 8 MeV high-resolution spectroscopy (SPI, Vedrenne et al. 2003). IBIS provides an angular resolution of 12′ full-width at half-maximum (*FWHM*) and an energy resolution, $E/\Delta E$, of ∼12 *FWHM* at 100 keV. SPI provides an angular resolution of 2.°5 *FWHM* and an $E/\Delta E$ of ∼430 *FWHM* at 1.3 MeV. The extremely broad energy range of IBIS is covered by two separate detector arrays, ISGRI (15–1000 keV, Lebrun et al. 2003) and PICsIT (0.175–10 MeV, Labanti et al. 2003). The payload is completed by X-ray (JEM-X, 3–35 keV, Lund et al. 2003) and optical monitors (OMC, *V*-band, Mas-Hesse et al. 2003). JEM-X has a fully coded FOV of 4.°8 diameter and an angular resolution of 3′ *FWHM*. All the instruments are co-aligned and are operated simultaneously.

As part of a Target of Opportunity programme on known black hole candidates, two INTEGRAL observations of the region of sky containing GRO J1655−40 were performed between 2005 March 18, 07:42 and 2005 March 19, 04:22 UTC, for a total time of 70 ks and between 2005 March 26, 19:00 and 2005 March 28, 00:56 UTC, for a total time of 100 ks, coinciding with the above mentioned XMM-Newton observations. The standard 5 × 5 dither patterns of pointings centered on the target were performed.

Data from the two observations were processed using the Off-line Scientific Analysis (OSA) version 5.1 software provided by the INTEGRAL Science Data Centre (ISDC, Courvoisier et al. 2003). This includes pipelines for the reduction of INTEGRAL data from all four instruments. The three high-energy instruments use coded masks to provide imaging information. This means that photons from a source within the field of view (FOV) are distributed over the detector area in a pattern

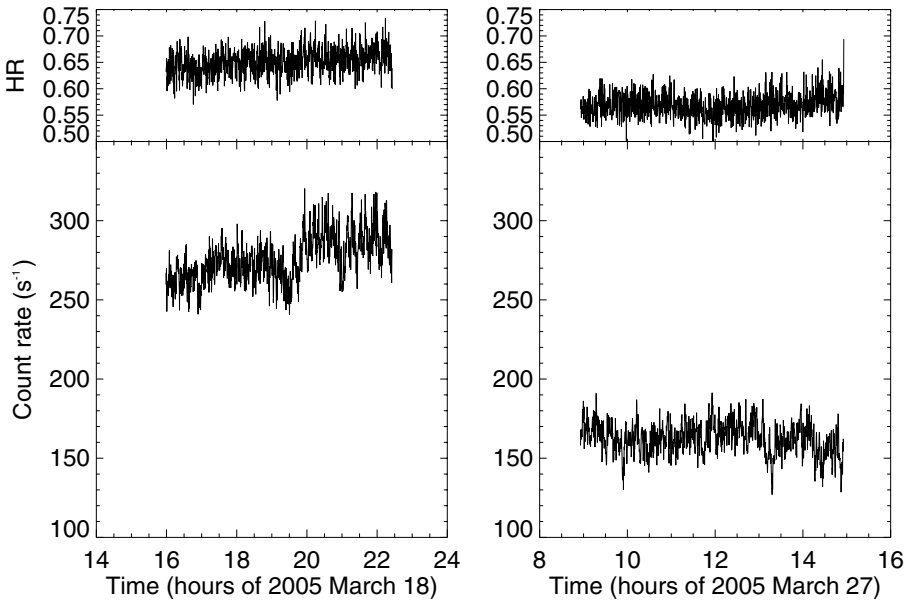

Fig. 2. *Lower panels*: 0.6–10 keV EPIC pn lightcurve of GRO J1655−40 for Obs 1 (*left panel*) and Obs 2 (*right panel*). The count rate has not been corrected for the 3% duty cycle of the burst mode. *Upper panels*: hardness ratio (counts in the 2.5–10 keV band divided by those between 0.6–2.5 keV) for Obs 1 (*left panel*) and Obs 2 (*right panel*). The binning is 20 s for all panels.

determined by the position of the source in the FOV. Source positions and intensities are determined by matching the observed distribution of counts with those produced by the mask modulation. In this paper we use data from JEM-X and ISGRI.

3. Results

3.1. Soft X-ray lightcurve

The EPIC pn 0.6–10 keV lightcurves from both observations are shown in Fig. 2 (lower panels) with a binning of 20 s. The upper panels show the hardness ratio (counts in the 2.5–10 keV energy range divided by those between 0.6–2.5 keV) also with a binning of 20 s. The source intensity increased from ∼260 count s^{-1} to ∼300 count s^{-1} during Obs 1. This increase is associated with an increase of the hardness ratio from 0.63 to 0.67, indicating that the source has not yet reached the outburst peak. In contrast, Obs 2 shows a lower count rate of ∼160 s^{-1} with no obvious trend present and a nearly constant hardness ratio. Strong variability is present during both observations. Although we do not plot the error bars in Fig. 2 for clarity, they are small compared to the average deviations seen. Two 10% and one 15% irregular reductions in intensity are present in Obs 1 and Obs 2, respectively.

3.2. X-ray spectra

We performed spectral analysis using XSPEC (Arnaud 1996) version 12.3.0. We used the photo-electric cross-sections of Wilms et al. (2000) to account for absorption by neutral gas with solar abundances (`tbabs` model in XSPEC). Spectral uncertainties are given at 90% confidence ($\Delta\chi^2 = 2.71$ for one parameter of interest), and upper limits at 95% confidence. We quote all line equivalent widths (*EW*s) with positive values for both absorption and emission features. We rebinned all spectra to oversample the *FWHM* of the energy resolution by a factor 3(5) for EPIC(RGS), and to have a minimum of 25 counts per bin, to allow the use of the χ^2 statistic. The systematic effects in the EPIC pn burst mode have been estimated as ∼5% (M. Kirsch, private communication). These effects are likely to be localized at low energies, mainly below 3 keV, and especially in the 1.5–3 keV energy band, where sharp drops at ∼1.9, 2.3 and 2.7 keV are present in the pn effective area. To account for such effects, we added quadratically a 5% uncertainty to each pn spectral bin in the 1.5–3 keV energy range and 2% in the rest of the energy band. We added 2% systematic uncertainty to the JEM-X and ISGRI spectra. In the following we present the results of fits to the RGS, EPIC pn, JEM-X and ISGRI spectra of GRO J1655−40 during the 2005 outburst[1].

3.2.1. Joint EPIC pn, JEM-X and ISGRI spectral analysis

We first fit the combined 0.5–10 keV EPIC pn, 5–20 keV JEM-X and 20–200 keV ISGRI spectra with a model consisting of a disk-blackbody and a power law, both modified by photo-electric absorption from neutral material (model `tbabs*(dbb+po)`). Constant factors, fixed to 1 for the EPIC pn spectra, but allowed to vary for the JEM-X and ISGRI spectra, were included multiplicatively in order to account for cross-calibration uncertainties. Previous RXTE and XMM-Newton spectra of GRO J1655−40 were fit with a multicolor disk-blackbody plus a power-law model with, or without, a cutoff (e.g., Ueda et al. 1998; Kuulkers et al. 1998; Tanaka et al. 2003). We note that, while a blackbody is a better fit to the low-energy part of the spectrum (0.5–10 keV), a disk-blackbody gives significantly better fits when the INTEGRAL 5–200 keV data are included. This is due to the fact that the high-energy data constrain the power-law component well, and consequently allow the other continuum components to be better studied.

The fits to the combined spectra with the `tbabs*(diskbb+po)` model are unacceptable with χ^2_ν of 9.3 and 19.0

[1] We note that for Obs 2 we have removed one bin between 20 and 30 keV which does not change the results of the fit but increases significantly the χ^2_ν. This bin may indicate a calibration feature or may have astrophysical origin. However, it is beyond the scope of this paper to analyse its nature and this will be done in a future paper about INTEGRAL data (Caballero-García et al., in preparation).

for 293 and 256 degrees of freedom (d.o.f.), for Obs 1 and Obs 2, respectively. The poor fit quality is mainly due to the presence of strong absorption features near 7 keV and strong emission features in the pn below 3 keV. A broad emission feature is superposed on the 7 keV absorption features. Structured residuals near 2.3 keV and 2.8 keV are probably due to an incorrect instrumental modeling of the Au mirror edges, whilst those near 1.8 keV are probably due to an incorrect modeling of the Si absorption in the CCD detectors. In addition, at the energies of these edges there is a sharp drop in the effective area of the pn. Both effects do not appear to be well accounted for in the EPIC pn calibration. An excess in the pn spectra is detected at ∼0.6 keV and can be modeled by a Gaussian emission line. This feature is present in both observations and could be emission from O VII. In addition, an absorption feature in the pn spectra is detected at ∼0.5 keV. Several absorption features are detected in the RGS at this energy and are attributed to O I and O II (see Sect. 3.2.2). Finally, an excess near 1 keV is detected in the EPIC pn spectrum in both observations. This feature is detected in a number of X-ray binaries and has been previously modeled either as an emission line, or as an edge, and its nature is unclear (e.g., Kuulkers et al. 1997; Sidoli et al. 2001; Boirin & Parmar 2003; Boirin et al. 2004, 2005). If the feature has an instrumental origin it might be expected to be stronger in the most luminous observation. The fact that the feature is very strong in the less luminous observation and only a weak excess is observed in Obs 1 could indicate that it has an astrophysical origin and its energy is consistent with a blend of Ne IX and Ne X emission, or Fe L emission.

We included a narrow Gaussian emission feature at 2.3 keV ($\texttt{gau}_5$) to account for the burst mode calibration deficiencies discussed previously. A Gaussian absorption line $\texttt{gau}_1$ was added to account for the absorption at ∼0.5 keV. The excesses at ∼0.6 keV and ∼1 keV were modeled by three Gaussian emission lines, $\texttt{gau}_{2-4}$. The first Gaussian accounts for the excess at 0.6 keV. The other two Gaussians account for the excess at 1 keV and their energies were fixed at 0.922 and 1.022 keV, the energies of Ne IX and Ne X resonance transitions. These additions reduce the χ^2_ν to 8.9 for 284 d.o.f for Obs 1 and to 8.7 for 247 d.o.f. for Obs 2.

To account for the complex residuals near 7 keV, absorption from a photo-ionized plasma (`warmabs` model within XSPEC) and a relativistic emission line (`laor`) modified by neutral absorption were added to the model. The `laor` model (Laor 1991) describes the line profile expected when an accretion disk orbiting a black hole with maximum angular momentum is irradiated by a source of hard X-rays. The χ^2_ν of the fit is significantly reduced to 1.5 for 276 d.o.f. and 2.1 for 239 d.o.f. for Obs 1 and Obs 2, respectively.

We substituted the relativistic emission line by a broad Gaussian emission line to check whether such a line may be broadened by effects other than relativity. The χ^2_ν of the fit increases, compared to the previous fit, to 9.3 for 278 d.o.f. for Obs 1 and to 9.3 for 241 d.o.f. for Obs 2. Thus, we conclude that relativistic broadening is more favoured than e.g. Compton scattering or the contribution from Fe with a range of ionization states for both observations. Finally we substituted the `laor` component by the `laor2` model in XSPEC, which uses a broken power-law emissivity profile instead of a power-law. The emissivity profile describes the dependence of the emissivity with radial position on the disk. This change reduces the χ^2_ν to 1.27 for 274 d.o.f. for Obs 1 and to 1.85 for 237 d.o.f. for Obs 2.

Table 1. Best-fits to the 0.5–10 keV EPIC pn, 5–20 keV JEM-X and 20–200 keV ISGRI spectra using the `tbabs*warmabs* (diskbb+po)` + `tbabs*(laor2+gau`$_1$`+gau`$_2$`+gau`$_3$`+gau`$_4$`)+gau`$_5$ `model`. $k_{\rm pl}$, $k_{\rm bb}$ and $k_{\rm gau}$ are the normalizations of the power law, disk-blackbody and Gaussian emission lines, respectively. $L_{0.5-200\ \rm keV}$ is the 0.5–200 keV luminosity for a distance of 3.2 kpc. The widths of the Gaussian emission lines $\texttt{gau}_{2-4}$ are constrained to be ≤0.1 keV.

	Obs 1	Obs 2
Parameter		
`po`		
Γ	2.23 ± 0.02	3.14 ± 0.02
$k_{\rm pl}$ [ph keV^{-1} cm^{-2} s^{-1} at 1 keV]	0.69 ± 0.04	4.5 ± 0.2
`diskbb`		
$kT_{\rm bb}$ [keV]	1.320 ± 0.003	1.303 ± 0.003
$k_{\rm bb}$ [($R_{\rm in}$ [km]/(D$_{10}$ [kpc]))^2 * cos θ]	849 ± 5	$434\ ^{+6}_{-3}$
`tbabs`		
$N_{\rm H}^{\rm abs}$ [10^{22} cm^{-2}]	$0.665\ ^{+0.002}_{-0.003}$	$0.77\ ^{+0.02}_{-0.01}$
`warmabs`		
$N_{\rm H}^{\rm warmabs}$ [10^{22} cm^{-2}]	5.2 ± 1.0	1.5 ± 1.2
log(ξ) [erg cm s^{-1}]	3.60 ± 0.04	3.30 ± 0.04
$\sigma_{\rm v}$ [km s^{-1}]	3500 ± 900	5900 ± 1200
`laor2`		
$E_{\rm gau}$ [keV]	6.60 ± 0.06	$6.80\ ^{+0.03}_{-0.05}$
$k_{\rm gau}$ [ph cm $^{-2}$ s^{-1}]	0.25 ± 0.02	0.226 ± 0.006
q_1	8.9 ± 0.2	$10\ _{-0.1}$
$r_{\rm in}$ [GM/c^2]	1.53 ± 0.02	1.37 ± 0.01
i [deg.]	52 ± 1	63.2 ± 0.2
q_2	$3.5\ ^{+0.5}_{-0.3}$	3.0 ± 0.3
$r_{\rm break}$ [GM/c^2]	3.6 ± 0.2	3.10 ± 0.09
$\texttt{gau}_1$		
$E_{\rm gau}$ [keV]	0.50 (f)	0.50 (f)
σ [keV]	0 (f)	0 (f)
$k_{\rm gau}$ [ph cm $^{-2}$ s^{-1}]	0.4 ± 0.2	2.0 ± 0.3
$\texttt{gau}_2$		
$E_{\rm gau}$ [keV]	0.60 (f)	0.60 (f)
σ [keV]	<0.02	<0.04
$k_{\rm gau}$ [ph cm $^{-2}$ s^{-1}]	0.3 ± 0.1	<0.4
$\texttt{gau}_3$		
$E_{\rm gau}$ [keV]	0.922 (f)	0.922 (f)
σ [keV]	0.1	$0.1\ _{-0.01}$
$k_{\rm gau}$ [ph cm $^{-2}$ s^{-1}]	<0.03	$0.25\ ^{+0.03}_{-0.05}$
$\texttt{gau}_4$		
$E_{\rm gau}$ [keV]	1.022 (f)	1.022 (f)
σ [keV]	$0.01_{-0.01}$	$0.1\ _{-0.01}$
$k_{\rm gau}$ [ph cm $^{-2}$ s^{-1}]	0.11 ± 0.03	0.27 ± 0.03
$\texttt{gau}_5$		
$E_{\rm gau}$ [keV]	2.28 ± 0.02	2.29 ± 0.03
σ [keV]	0 (f)	0 (f)
$k_{\rm gau}$ [ph cm $^{-2}$ s^{-1}]	0.039 ± 0.008	0.008 ± 0.004
χ^2_ν	1.27	1.85
d.o.f.	274	237
Exposure EPIC pn [ks]	0.69	0.64
$L_{0.5-200\ \rm keV}$ [10^{37} erg s^{-1}]	7.68	3.95

The parameters of the best-fit model (model 1: `tbabs* warmabs*(diskbb+po)` + `tbabs*(laor2+gau`$_1$`+gau`$_2$`+gau`$_3$`+gau`$_4$`)+gau`$_5$) are given in Table 1. Figure 3 shows the best-fit model and residuals and Fig. 4 the components of the model. We have checked for the presence of a cutoff in the power-law component by including a high-energy cutoff and calculating the 90% confidence limits. We find no evidence of a break in the power-law component up to energies of 380 keV and 90 keV for Obs 1 and Obs 2, respectively.

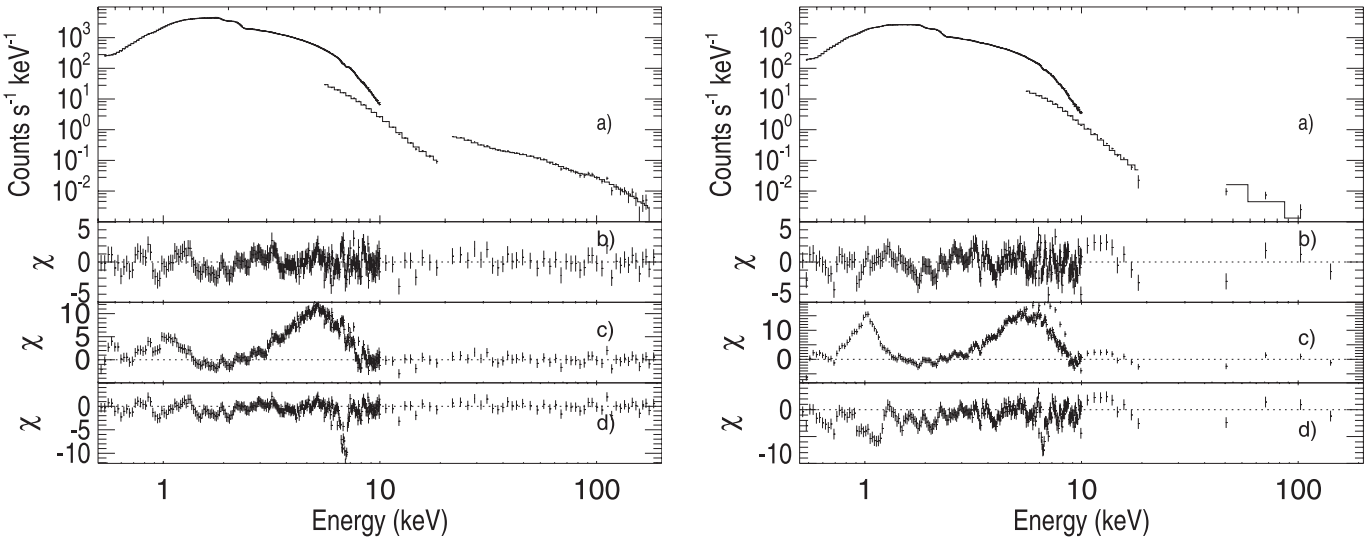

Fig. 3. a) GRO J1655−40 EPIC pn, JEM-X and ISGRI spectra from Obs 1 (*left*) and Obs 2 (*right*) fit with a model consisting of disk-blackbody (dbb) and power-law (po) components modified by absorption from neutral (tbabs) and ionized (warmabs) material together with a relativistic emission line (laor2), four emission Gaussians (gau_{1-4}) modified by absorption from neutral material (tbabs) and a Gaussian (gau_5) to account for calibration uncertainties. **b)** Residuals in units of standard deviation from the above model. **c)** Residuals when the normalisations of the laor2 component, and the Gaussians are set to 0. The laor2 component indicates relativistic broadening. **d)** Residuals when $N_{\rm H}^{\rm warmabs}$ is set to 0. Absorption lines are clearly visible near 7 keV. The best-fit parameters are given in Table 1.

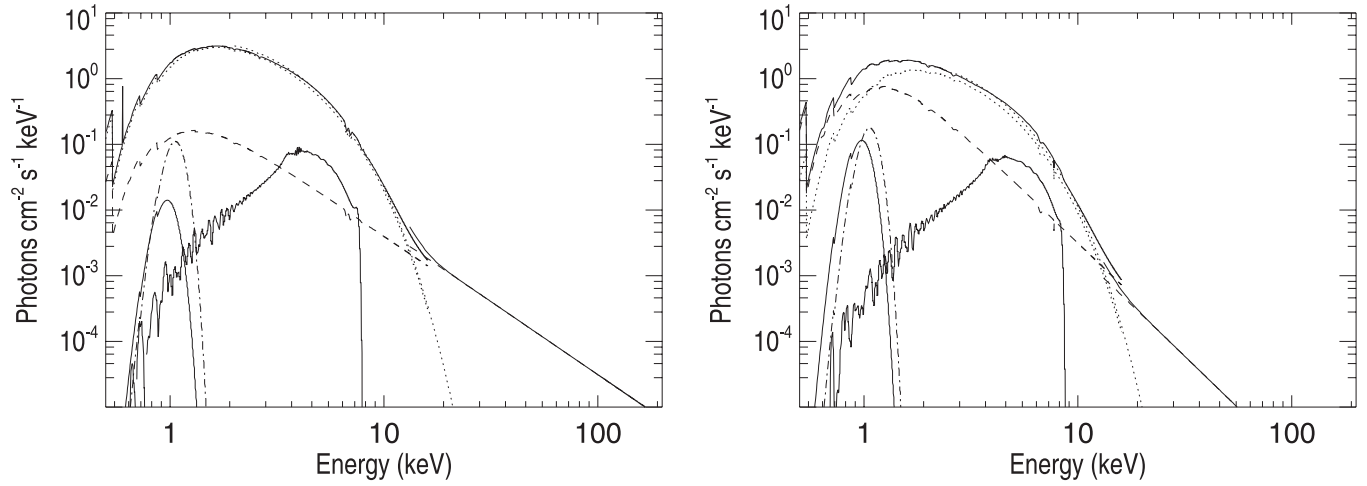

Fig. 4. GRO J1655−40 photon spectrum during Obs 1 (*left panel*) and Obs 2 (*right panel*) with the separate components indicated: disk-blackbody (dotted line), power-law (dashed line), laor2 relativistic line (dot-dashed line) and soft excess at 1 keV (three dots-dashed line). The best-fit parameters are given in Table 1.

Next, we added a blurred reflection component (`kdblur*pexriv` in XSPEC) to model 1. This component calculates the Compton-reflected continuum but not the Fe Kα line. Thus we continued using the relativistic line of the previous fits. The fits do not improve significantly compared to the fits without reflection and the amount of reflection is unconstrained. Further, the reflection component cannot account for the excess observed at 1 keV mainly during Obs 2. Finally, we substituted the power-law and `pexriv` components by the constant density ionized disk reflection model (`reflion.mod` component in XSPEC). This model measures the relative strengths of the directly observed and reflected flux, the accretion disk ionization parameter ξ and the photon index of the illuminating power-law flux. Fe Kα line emission and line broadening due to Comptonization in an ionized disk surface layer are included in this model. The fits do not improve significantly compared to the fits without reflection and the strong relativistic lines present in both observations cannot be accounted for by this component. However we note that, if included in addition to the relativistic line and the power-law component, the `reflion` component can account for the excess at 1 keV in Obs 2, and the fit is improved significantly with a final χ^2_ν of 1.70 for 234 d.o.f.. The reflection is ionized with $\log(\xi) = 3.4$ and a overabundance of Fe of 2.8 with respect to the solar value is found. The blurring of the reflection component indicates a different area of reflection with respect to the relativistic line. In the case of reflection, the values of the inner radius, the emissivity and the inclination are 1.86 GM/c^2, 10 and 75° respectively. No acceptable fit is found when the parameters of the relativistic blurring are linked for the reflection component and the relativistic line.

We conclude that the best-fit to the EPIC pn, JEM-X and ISGRI spectra is model 1. The continuum can be well described by a power law with a photon index, Γ, of ∼2.2–3.1 and a disk-blackbody with a temperature, $kT_{\rm bb}$, of ∼1.3 keV.

The contribution of the power law to the total 2–10 keV luminosity is ≲4% and ≲10% for Obs 1 and Obs 2, respectively. The hydrogen column density, $N_{\rm H}^{\rm abs}$, is 0.7–0.8 × 10^{22} atom cm^{-2}. We can compare these values to those obtained from *Swift* observations (see Tables 4 and 5 of Brocksopp et al. 2006). The *Swift* observation 00030009005 was taken ∼8 h later than XMM-Newton Obs 1. It shows a similar value of $N_{\rm H}^{\rm abs}$ ($0.69^{+0.01}_{-0.02}$ × 10^{22} atom cm^{-2}), a significantly smaller power-law index (Γ = 1.7 ± 0.1) and a similar temperature for the disk ($kT_{\rm bb}$ = 1.36 ± 0.02). The *Swift* observation 00030009008 was simultaneous with the XMM-Newton Obs 2. It shows similar values of $N_{\rm H}^{\rm abs}$ (0.78 ± 0.03 × 10^{22} atom cm^{-2}) and power-law index (Γ = 3.3 ± 0.2) and a higher disk temperature ($kT_{\rm bb}$ = $1.56^{+0.01}_{-0.02}$). The absence of a photo-ionized absorber and relativistic Fe K emission in the modeling of the *Swift* spectra probably contributes to these differences.

A relativistic emission feature centered on 6.60–6.80 keV is detected in both XMM-Newton observations at a confidence level >8σ, as determined by an F-test [2]. We obtained better fits modeling the broadening of the line with a `laor2` component compared to the `laor` component and to the Gaussian broadening for both observations. The inclination of the `laor2` component is defined as the angle between the line of sight and the rotation axis of the disk and was allowed to vary between 50 and 90°, since the inclination of the disk has been determined to be 70° for GRO J1655−40. The inner radius for the emitting region has a value of 1.4–1.5 in units of GM/c^2, indicating that the line is emitted very close to the horizon of a Kerr black hole. The outer radius has been left fixed to the initial value of 400 during the fits. The emissivity profile is best described by a broken power-law, with q_1 = 9–10 within the break radius $r_{\rm break}$ = 3.6–3.1 and q_2 = 3.5–3.0 at larger radii. The steep emissivity indicates that the disk is illuminated mostly in its very inner regions supporting the idea that the primary source is very close to the black hole. It is not possible to fit the emission line unless we allow a very large emissivity. Comparable emissivity indices (∼7) have been observed from a number of Seyfert galaxies (e.g., Fabian et al. 2004, 2005) and are indicative of a primary source very close to the black hole.

We measured the *EW* of the Fe XXV and Fe XXVI absorption features and edges produced by the warm absorber by removing the warm absorber component and adding individually Gaussian absorption features and edges to the model. The results are shown in Table 2 and a detail of the absorption features in Fig. 5. During Obs 1, the *EW* of the Fe XXV absorption feature is smaller than that of the Fe XXVI Lyα feature, whilst the opposite occurs for Obs 2, indicating a less ionized absorber. For Obs 2, the *EW*s are larger for the Lyβ compared to the Lyα features. This indicates that the Fe XXV Lyβ feature is rather a blend of Fe XXV Lyβ and Ni XXVII, while the Fe XXVI Lyβ feature is a blend of Fe XXVI Lyβ and Ni XXVIII.

Table 2. Best-fit of the most prominent EPIC pn absorption features with negative Gaussian profiles for the two observations of GRO J1655−40 using XSPEC. The σ of the narrow Gaussian absorption features are constrained to be <0.1 keV.

	Obs 1		Obs 2	
Lines				
	Fe XXV		Fe XXV	
	Kα	Kβ	Kα	Kβ
$E_{\rm gau}$ [keV]	6.68 ± 0.03	$7.88^{+0.16}_{-0.11}$	6.64 ± 0.02	7.78 ± 0.05
σ [keV]	$0.1_{-0.06}$	$0^{+0.1}$	0.06 ± 0.03	$0.1_{-0.07}$
EW [eV]	33 ± 9	11 ± 8	32 ± 6	36 ± 15
	Fe XXVI		Fe XXVI	
	Kα	Kβ	Kα	Kβ
$E_{\rm gau}$ [keV]	6.96 ± 0.02	$8.13^{+0.06}_{-0.20}$	6.98 ± 0.04	$8.12^{+0.02}_{-0.03}$
σ [keV]	0.06 ± 0.03	$0^{+0.1}$	$0^{+0.1}$	<0.07
EW [eV]	39 ± 11	8 ± 4	18^{+6}_{-9}	42^{+14}_{-28}
Edges				
	Fe XXV		Fe XXV	
$E_{\rm edge}$ [keV]	8.96 ± 0.40		$8.74^{+0.03}_{-0.10}$	
τ	<0.06		0.18 ± 0.02	
	Fe XXVI		Fe XXVI	
$E_{\rm edge}$ [keV]	9.278 (f)		9.278 (f)	
τ	<0.05		<0.02	

3.2.2. RGS spectral analysis

Next, we examined the 30 RGS1 spectra (first and second order taken sequentially between 0.3 and 1.9 keV). The RGS2 spectra were strongly piled-up and were therefore not used in the fits (see Sect. 2). We note that the joint analysis of RGS and pn data was not possible due to the presence of strong emission features in the pn below 3 keV which were not detected in the overlapping energy range of the RGS (see Sect. 3.2.1) and to the presence of detailed structure at the interstellar O K and Fe L edges in the RGS (see below) which was not resolved in the pn. We could fit the RGS1 spectra of both observations with a continuum consisting of a power law modified by photoelectric absorption from neutral material (χ^2_ν of 1.60 and 1.67 for 2183 and 2167 d.o.f. for Obs 1 and Obs 2, respectively). The RGS spectra show structured residuals near the O edge at ∼0.54 keV. Around this energy there is a significant change (∼25%) in the instrument efficiency, which may not be fully accounted for in the data processing. Thus, the residuals could be due either to a calibration uncertainties or have an astrophysical origin. We checked for the second possibility by studying in detail the region around 0.54 keV. We searched for the signature of O absorption in the interstellar medium similar to that observed by Takei et al. (2002) and Costantini et al. (2005) from Cyg X-2 and by Juett et al. (2004) from a number of sources.

We included narrow Gaussian absorption features at energies of 0.498, 0.527 and 0.534 keV for Obs 1 and 0.488, 0.511 and 0.528 keV for Obs 2 (see Fig. 6). This improves the fit significantly and we identify the common feature at 0.528 keV with absorption from O I and the feature at 0.534 keV in Obs 2 with absorption from O II. We can not identify the other absorption features found without assigning them extremely high velocity shifts. However, we note that, if these features are of interstellar origin, such velocity shifts are not expected for galactic sources. A more plausible explanation is that at the low detected count rates, data binning may cause several lines to blend (see the extreme blending of the lines in Obs 2 compared to Obs 1 in Fig. 6). Thus, the energy of the detected lines should be regarded rather as an average of the various O lines present (see e.g., Juett et al. 2004). In addition, two absorption features at 0.711 keV and 0.720 keV are evident in the first and second order RGS spectra of the two observations. We attribute these features to absorption by interstellar Fe in the L3 ($2p_{3/2}$) and L2 ($2p_{1/2}$) edges, respectively. Including narrow Gaussian absorption features to model these residuals reduces the χ^2_ν to 1.53 for 2168 d.o.f for Obs 1 and to 1.53 for 2152 d.o.f. for Obs 2. The energies and

[2] We note that we use the F-test only as an indication for the significance of the feature. For more realistic estimations, simulations are required (see Protassov et al. 2002).

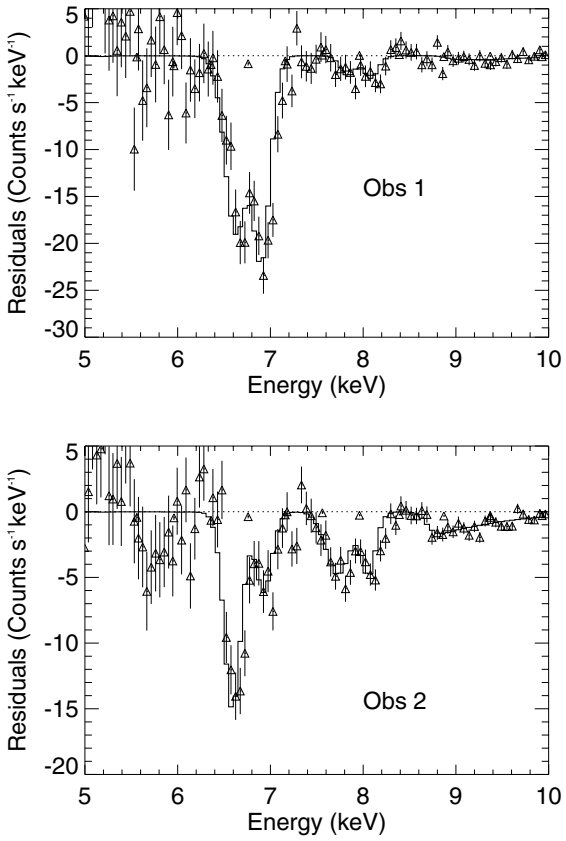

Fig. 5. GRO J1655−40 5–10 keV EPIC-pn spectral residuals from the best-fit `tbabs*edge*edge*(dbb+po+gau`$_6$`+gau`$_7$`+gau`$_8$`+gau`$_9$`)+tbabs*(laor2+gau`$_1$`+gau`$_2$`+gau`$_3$`+gau`$_4$`)+gau`$_5$ model when the normalizations of the Gaussian absorption features `gau`$_{6-9}$ and the edges are set to zero.

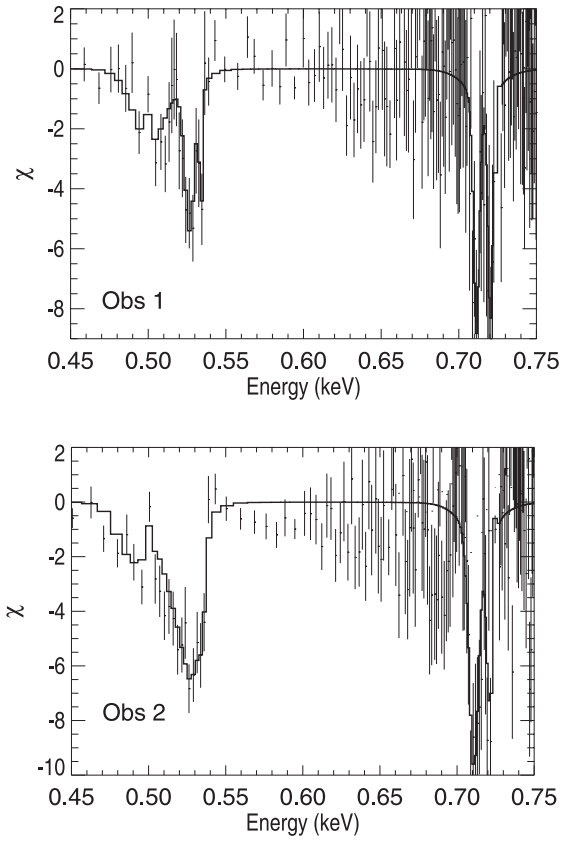

Fig. 6. GRO J1655−40 0.45–0.75 keV RGS spectral residuals from the best-fit model (`tbabs*(pl+gau+gau+gau+gau+gau)` for Obs 1 and `tbabs*warmabs*(pl+gau+gau+gau+gau+gau)` for Obs 2) when the normalizations of the Gaussian absorption features are set to zero.

equivalent widths of all the detected features are listed in Table 3. The residuals of the best-fits to the RGS spectra when such lines are excluded are shown in Fig. 6.

The Obs 1 spectra do not show any apparent features except for the ones previously mentioned and including absorption from a photo-ionized plasma in the model does not improve the quality of the fit. In contrast, the Obs 2 spectra show a number of low intensity absorption features superposed to the continuum, in addition to the ones attributed to absorption in the interstellar medium. To account for these features absorption from a photo-ionized plasma (component `warmabs` in XSPEC) was added to the model. An ionized absorber with $N_{\rm H}^{\rm warmabs} = (3.2 \pm 1.6) \times 10^{22}$ atom cm^{-2}, $\log(\xi) = 3.3 \pm 0.1$, $\sigma_{\rm v} = 160 \pm 60$ km s^{-1} and $v = -540 \pm 120$ km s^{-1} fits well the absorption features and the final χ^2_ν is 1.45 for 2148 d.o.f (note that we keep here the parameters of the continuum fixed to the values of the previous fit). Figure 7 shows the best-fit model to the RGS spectra of Obs 2. The lines are significantly blue-shifted, indicating that the absorbing matter is an outflow along our line of sight. The blue-shift detected in the RGS spectra which have an energy resolution of ∼300 at 1 keV, is too small to be detected with the pn camera, which has an energy resolution of ∼45 at 6.4 keV and is only sensitive to shifts $\gtrsim$1000 km s^{-1}. Two narrow absorption features are detected at 1.023 ± 0.002 and 1.168 ± 0.002 keV with *EW*s of <1 eV and 4.3 ± 1.2 eV and are identified with Ne X and Fe XXIV, respectively. The column density and photo-ionization parameter of the absorber are consistent within the uncertainties with the absorber fit to the pn spectrum, showing that the same outflow is able to produce the Ne X and Fe XXIV features at ∼1 keV and the highly ionized Fe XXV and Fe XXVI features at ∼7 keV.

We next fitted the abundances of O, Ne and Fe, which were previously fixed at solar values. We obtained values of <0.8, 5^{+3}_{-4} and 4 ± 3 for O, Ne and Fe, respectively, with respect to solar values. The parameters of the ionized absorber are fixed during the fit of the abundances and the fit is improved, but not significantly, with a final χ^2_ν of 1.44 for 2142 d.o.f. Thus, we find no evidence for a significant overabundance of any element, with respect to solar values. Unusual Ne/O abundance ratios have been reported for several ultracompact X-ray binaries and have been attributed to a donor rich in Ne (e.g, Juett & Chakrabarty 2003). Variations in the Ne/O abundance ratio may be related to ionization effects due to continuum spectral variations (see Juett & Chakrabarty 2005, and references therein). We note that using a self-consistent model for the photo-ionized absorber, no significant Ne/O overabundance is detected in the RGS spectra.

3.3. Time-resolved spectral fits during Obs 1

As Fig. 2 shows, both the flux and hardness ratio of GRO J1655−40 increased during Obs 1. To study the variations of the highly-ionized absorber with the increase in flux, we divided the light curve of Obs 1 into two segments. We extracted two RGS spectra, set 1 comprises from the beginning till the middle of the observation and set 2 from the middle till the end, since the middle "dip" interval had very few counts.

Table 3. Best-fit of the most prominent RGS absorption features with negative Gaussian profiles for the two GRO J1655−40 observations. The fits were performed using XSPEC on the RGS spectra. f indicates that a parameter was fixed during the fitting. The σ of the narrow Gaussian absorption features is constrained to be <0.01 keV.

Obs 1			Obs 2		
$E_{\rm gau}$ [keV]	σ [keV]	EW [eV]	$E_{\rm gau}$ [keV]	σ [keV]	EW [eV]
$0.498\ ^{+0.011}_{-0.003}$	$0.010\ ^{}_{-0.002}$	$14\ ^{+5}_{-3}$	$0.488\ ^{+0.004}_{-0.008}$	$0.010\ ^{}_{-0.002}$	19 ± 5
0.527 ± 0.003	0.003 ± 0.001	$9\ ^{+4}_{-3}$	$0.511\ ^{+0.003}_{-0.006}$	0.006 ± 0.004	$7\ ^{+6}_{-3}$
0.534 ± 0.004	<0.01	<6	$0.528\ ^{+0.002}_{-0.004}$	$0.009\ ^{+0.007}_{-0.002}$	$23\ ^{+7}_{-3}$
0.711 ± 0.001	<0.003	3 ± 1	0.711 ± 0.002	<0.004	5 ± 3
0.720 ± 0.001	<0.003	2 ± 1	$0.721\ ^{+0.002}_{-0.005}$	<0.006	$2\ ^{+5}_{-1}$
			1.023 ± 0.002	<0.002	<1
			1.168 ± 0.002	0.003 ± 0.002	4.3 ± 1.2

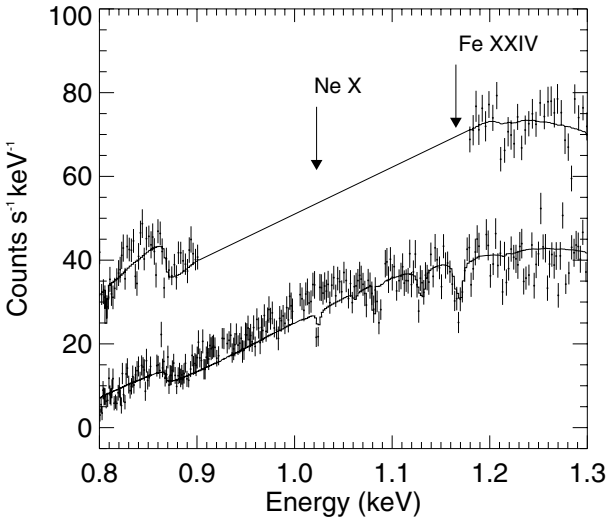

Fig. 7. First and second order RGS1 GRO J1655−40 spectra of Obs 2. Two narrow absorption features are detected at 1.023 ± 0.002 and 1.168 ± 0.002 keV and identified with Ne X and Fe XXIV, respectively.

Both sets can be fit with the same model as for the complete observation which is a continuum consisting of a power law modified by photo-electric absorption from neutral material (χ^2_ν of 1.41 and 1.44 for 1865 and 1971 d.o.f. for first and second sets, respectively). The power-law index is the same for both observations ($\Gamma = 1.38$). Similarly, the column density of the neutral absorption, $N_{\rm H}$, does not change significantly from the first ($N_{\rm H} = (7.60 \pm 0.05) \times 10^{21}$ cm^{-2}) to the third set ($N_{\rm H} = (7.7 \pm 0.1) \times 10^{21}$ cm^{-2}). Including absorption by an ionized slab into the model does not improve the fit significantly for either set.

4. Discussion

We have analysed two observations of GRO J1655−40 during its 2005 outburst. During Obs 1, which occurs close to the maximum of the first peak of the outburst, the 0.5–10 keV luminosity is still increasing, and it is clearly in the high-soft state, showing an X-ray emission dominated by the thermal emission (the 2–10 keV luminosity is $\gtrsim$96%), probably from the optically thick accretion disk, and a weak, steep hard X-ray power law. Obs 2 is close to the minimum of the first peak of the outburst, nine days later, and shows a lower, less-variable luminosity. However the characteristics of the source still resemble those of a high-soft state. The absence of quasi-periodic oscillations (QPOs) in the RXTE data from 2005 March 18 between 19:41 and 21:41 UTC and from 2005 March 27 between 07:46 and 11:56 UTC, simultaneous to the analyzed XMM-Newton and INTEGRAL first and second observations, respectively, indicate that GRO J1655−40 is not in the "steep power law" state, as defined by McClintock & Remillard (2006), but rather in the high-soft state, where the power law is weak (less than 10% of the total 2–10 keV luminosity) and has indices between 2.1 and 4.8, and QPOs are absent in the power spectrum.

A highly-ionized absorber is observed superposed on the continuum in both observations. The absorber is less ionized and has a smaller column density during Obs 2, where blueshifted absorption features of Ne X and Fe XXIV are detected in the 0.3–1.9 keV RGS spectrum, in addition to the EPIC pn Fe XXV and Fe XXVI features. A range of absorbers with different temperature or density is not required to explain the features at ∼7 keV and below 2 keV. Presumably, the ionized absorber is an outflow in both observations, but we can only give upper limits (the EPIC pn energy resolution is ∼1000 km s^{-1} at 6 keV) to the outflow velocity in Obs 1 due to the absence of features in the RGS spectrum. The relation of luminosity of the X-ray source with the accretion rate has been extensively discussed (e.g., Hynes et al. 1998). In the case that the lower luminosity during Obs 2 indicated that the accretion rate was smaller, the absorber column could be related to the accretion rate. Further, the value of the ionization parameter of the absorber is directly related to the luminosity ($\xi = L/n_{\rm e}r^2$). Therefore a lower degree of ionization is expected in Obs 2, which has a lower luminosity, as detected.

Narrow X-ray absorption lines from highly ionized Fe were first detected in superluminal jet sources (Ueda et al. 1998; Yamaoka et al. 2001; Kotani et al. 2000; Lee et al. 2002) and subsequently in an increasing number of low-mass X-ray binaries observed by XMM-Newton (Ueda et al. 2001; Díaz Trigo et al. 2006, and references therein). Recently, *Chandra* HETGS observations of the black hole candidates GX 339−4, XTE J1650−500 and H 1743−322 (Miller et al. 2004, 2006b) have revealed the presence of variable, blueshifted, highly-ionized absorption features which are interpreted as evidence for outflows.

The detection of an outflowing highly-ionized absorber in GRO J1655−40 confirms that the outflowing winds present in AGNs are also a common feature of microquasars. In contrast, no blueshifts have been detected in any of the highly-ionized absorbers present in dipping LMXBs (Díaz Trigo et al. 2006). However, these results are all obtained with the EPIC pn, which has a factor ∼4 poorer resolution than the HETGS at 6 keV limiting the sensitivity to shifts $\gtrsim$1000 km s^{-1}. Therefore, we calculated the upper limits for the velocity shift in MXB 1658−298, the only LMXB which shows absorption features of O VIII and

Ne X in the RGS. We obtain a velocity shift of -215^{+245}_{-270} km s^{-1} for the absorber, indicating only a marginal blueshift. Attempts have been made to relate the ionized absorption with jet emission, first due to the discovery of absorbers in microquasars preceding the discovery in LMXBs (e.g., Ueda et al. 1998), and later due to the difference in velocity shift between both kinds of systems, i.e. an outflowing wind in microquasars versus an static atmosphere in LMXBs (Miller et al. 2006b).

The detection of ionized absorbers in many highly-inclined systems points to a common origin for the absorbers in LMXBs and microquasars, and not related to the jets of the latter. Further, with the data available up to now we can not exclude a velocity shift in the absorbers of LMXBs, which marks a difference between the absorbers in galactic black holes and LMXBs. Measurements of shifts of low ionized features with the RGS on-board XMM-Newton or HETGS on-board *Chandra* are necessary in order to gain insight into the distribution and origin of the ionized absorbers. The detection of a different column density and ionization state of the absorber in different phases of the outburst establishes a clear link between the variability of the warm absorber and the central accretion engine. This link is confirmed when comparing the highly-ionized absorption lines detected by ASCA (Ueda et al. 1998) with the ones shown in Table 2: an increase in the flux from the "low-state" ASCA observation to XMM-Newton Obs 2 and Obs 1 and finally to the "high-state" ASCA observation is accompanied by an increase of the ionization parameter, ξ. While only Fe XXV features are detected in the "low-state" ASCA observation, both Fe XXV and Fe XXVI are seen in the XMM observations and only a Fe XXVI feature remains in the "high-state" ASCA observation. The long dynamical time scales make it difficult to perform studies of variability of the warm absorber with the central accretion engine in AGNs. Thus future observations of galactic black holes may also provide insights in accretion processes in AGNs.

A relativistically broadened Fe Kα emission line is detected in both observations. The inner emission radius of the line is smaller than $6R_{\rm g}$, indicating that GRO J1655−40 harbors a black hole with significant spin. A further indication of the existence of a spinning black hole in GRO J1655−40 is the presence of high-frequency QPOs (Strohmayer 2001; Abramowicz & Kluzniak 2001). All the parameters of the line, except the emissivity, are consistent with the relativistically broadened Fe Kα line previously detected by ASCA (Miller et al. 2005). The energies of the lines, 6.60 and 6.80 keV, are consistent with ionized emission from Fe XXV and lower ionization stages from Fe, such as Fe XXIV and Fe XXIII for Obs 1, and from Fe XXV and Fe XXVI for Obs 2. Ionized Fe K emission is expected from a disk with such a high temperature ($kT \sim 1.3$ keV). The discrepancy in the emissivity, ∼9–10 in our observations compared to ∼5.5 in ASCA observations, may be a consequence of the model chosen to perform the fits. The spectra fit in this paper show highly ionized absorption lines, which are modeled with a photo-ionized absorber. The absorption is strong, $N_{\rm H}^{\rm xabs} = (5.2 \pm 1.0)$ and $(1.5 \pm 1.0) \times 10^{22}$ atom cm^{-2} for Obs 1 and 2, respectively, and causes a change in the continuum. The relativistic emission line occurs at the same energy interval than the strongest absorption lines and edges, and therefore an absent or deficient modeling of the absorption (e.g. by including the lines and edges independently) will vary the parameters of the emission feature. Further, the ASCA fits include a smeared edge at 8 keV to simulate reflection from the disk. This edge is not included in our fits. Finally, the inclination in the ASCA fits (45^{+15}_{-5} degrees), though consistent within the errors, is lower than the one in our fits (52 ± 1 and 63.2 ± 0.2 degrees). This may explain partially the high emissivity of our fits ($q_1 \sim 9$–10), since an increase in the emissivity produces the same effect as a lower inclination in the relativistic line. The simultaneous modeling of the absorption features and of the relativistic Fe K emission line is crucial in order to obtain realistic values for the parameters of the model. It has been argued (e.g., Done & Gierlinski 2006) that relativistic smearing can be significantly reduced if there is also Fe K line absorption from an outflowing disk wind. We find that *both* an extremely relativistic emission line, confirming the existence of a spinning black hole, and strong ionized absorption are present in the outburst spectra of GRO J1655−40.

The role of reflection and absorption in AGNs has been extensively discussed (e.g., Chevallier et al. 2006). The reflection models used in our fits cannot account for the strong relativistic Fe K line and do not improve significantly the fits. Further, they can not explain either the strong excess at 1 keV of Obs 2, unless the region of reflection is different to the region of emission of the relativistic line, an extra power-law component is included and an overabundance of 2.8 of Fe with respect to solar values is allowed. A narrow emission line is observed at 0.6 keV in Obs 1. Such line at 0.6 keV could be associated to emission from O VII, if its astrophysical origin is confirmed. However, its non-detection in the RGS data may indicate that the line has an instrumental origin. The feature at 1 keV, detected at high significance in Obs 2, and only marginally in Obs 1, has been observed in other sources and its origin is unclear. The fact that it is stronger in the less luminous GRO J1655−40 observation indicates that it could have an astrophysical origin. In that case, it could be related to a combination of Ne IX and Ne X or the Fe L complex.

One month after submission of this paper to A&A, a paper by Miller et al. (2006a) reporting on a *Chandra* observation of GRO J1655−40 performed on 1 April 2005, 5 days after Obs 2, was accepted for publication. The HETGS spectrum shows 90 absorption lines significant at the 5σ significance level or higher, from which 76 are identified with resonance lines expected from over 32 charge states. The equivalent widths of the lines detected by *Chandra* are a factor ∼1.5 larger than the ones of the corresponding lines detected in XMM-Newton Obs 2. This indicates an increase in the column density of the absorber from the XMM-Newton Obs 2 to the *Chandra* observation. This change in the column density and the difference in exposure times, 0.64 ks(1.8 ks) in the pn(RGS) for Obs 2 versus 63.5 ks in the HETGS, explain the detection of

significantly fewer lines in the XMM-Newton observation.

Acknowledgements. Based on observations obtained with XMM-Newton, an ESA science mission with instruments and contributions directly funded by ESA member states and the USA (NASA), and on observations with INTEGRAL, an ESA project with instruments and science data centre funded by ESA member states (especially the PI countries: Denmark, France, Germany, Italy, Switzerland and Spain), Czech Republic and Poland, and with the participation of Russia and USA. M. Díaz Trigo acknowledges an ESA Research Fellowship. We thank the RXTE instrument teams at MIT and NASA/GSFC for providing the ASM lightcurve. We thank the anonymous referee for helpful comments. M. Díaz Trigo thanks Tim Kallman for his help with the `warmabs` model. M. D. Caballero-García is funded by MEC ESP2005-07714-C03-03.

References

Abramowicz, M. A., & Kluzniak, W. 2001, A&A, 374, L19
Arnaud, K. A. 1996, in Astronomical Data Analysis Software and Systems V, ASP Conf. Ser., 101, 17
Balucińska-Church, M. 2001, Adv. Space Res., 28, 349
Boirin, L., & Parmar, A. N. 2003, A&A, 407, 1079
Boirin, L., Parmar, A. N., Barret, D., Paltani, S., & Grindlay, J. E. 2004, A&A, 418, 1061

Boirin, L., Méndez, M. Díaz Trigo, M., Parmar, A. N., & Kaastra, J. 2005, A&A, 436, 195
Brocksopp, C., McGowan, K. E., Krimm, H., et al. 2006, MNRAS, 365, 1203
Chevallier, L., Collin, S., Dumont, A. M., et al. 2006, A&A, 449, 493
Costantini, E., Freyberg, M. J., & Predehl, P. 2005, A&A, 444, 187
Courvoisier, T. J.-L., Walter, R., Beckmann, V., et al. 2003, A&A, 411, L53
Den Herder, J. W., Brinkman, A. C., Kahn, S. M., et al. 2001, A&A, 365, L7
Díaz Trigo, M., Parmar, A. N., Boirin, L., Mendez, M., & Kaastra, J. 2006, A&A, 445, 179
Done, C., & Gierlinski, M. 2006, MNRAS, 367, 659
Fabian, A. C., Miniutti, G., Gallo, L., et al. 2004, MNRAS, 353, 1071
Fabian, A. C., Miniutti, G., Iwasawa, K., & Ross, R. R. 2005, MNRAS, 361, 795
Hjellming, R. M., & Rupen, M. P. 1995, Nature, 375, 464
Homan, J. 2005, The Astronomer's Telegram, 440, 1
Hynes, R. I., Haswell, C. A., Shrader, C. R., et al. 1998, MNRAS, 300, 64
Jansen, F., Lumb, D., Altieri, B., et al. 2001, A&A, 365, L1
Juett, A. M., & Chakrabarty, D. 2003, ApJ, 599, 498
Juett, A. M., & Chakrabarty, D. 2005, ApJ, 627, 926
Juett, A. M., Schulz, N. S., & Chakrabarty, D. 2004, ApJ, 612, 308
Kotani, T., Ebisawa, K., Dotani, T., et al. 2000, ApJ, 539, 413
Kuulkers, E., Parmar, A. N., Owens, A., Oosterbroek, T., & Lammers, U. 1997, A&A, 323, L29
Kuulkers, E., Wijnands, R., Belloni, T., et al. 1998, ApJ, 494, 753
Kuulkers, E., in't Zand, J. J. M., Cornelisse, R., et al. 2000, A&A, 358, 993
Labanti, C., Di Cocco, G., Ferro, G., et al. 2003, A&A, 411, L149
Laor, A. 1991, ApJ, 376, 90
Lebrun, F., Leray, J. P., Lavocat, P., et al. 2003, A&A, 411, L141
Lee, J. C., Reynolds, C. S., Remillard, R., et al. 2002, ApJ, 567, 1102
Lund, N., Budtz-Jørgensen, C., Westergaard, N. J., et al. 2003, A&A, 411, L231
Maccarone, T. J. 2002, MNRAS, 336, 1371
Markwardt, C. B., & Swank, J. H. 2005, The Astronomer's Telegram, 414, 1
Mas-Hesse, J. M., Giménez, A., Culhane, J. L., et al. 2003, A&A, 411, L261
McClintock, J. E., & Remillard, R. A. 2006, in Compact Stellar X-ray Sources, ed. W. H. G. Lewin, & J. van Paradijs (Cambridge University Press)
Miller, J. M., Raymond, J., Fabian, A. C., et al. 2004, ApJ, 601, 450
Miller, J. M., Fabian, A. C., Nowak, M. A., & Lewin, W. H. G. 2005, Proc. of the Tenth Marcel Grossman Meeting on General Relativity
Miller, J., Raymond, J., Fabian, A., et al. 2006a, Nature, 441, 953
Miller, J. M., Raymond, J., Homan, J., et al. 2006b, ApJ, 646, 394
Orosz, J. A., & Bailyn, C. D. 1997, ApJ, 477, 876
Protassov, R., van Dyk, D. A., Connors, A., Kashyap, V. L., & Siemiginowska, A. 2002, ApJ, 571, 545
Shahbaz, T., van der Hooft, F., Casares, J., Charles, P. A., & van Paradijs, J. 1999, MNRAS, 306, 89
Sidoli, L., Oosterbroek, T., Parmar, A. N., Lumb, D., & Erd, C. 2001, A&A, 379, 540
Strüder, L., Briel, U., Dennerl, K., et al. 2001, A&A, 365, L18
Strohmayer, T. E. 2001, ApJ, 552, L49
Takei, Y., Fujimoto, R., Mitsuda, K., & Onaka, T. 2002, ApJ, 581, 307
Tanaka, Y., Ueda, Y., & Boller, T. 2003, MNRAS, 338, L1
Tingay, S. J., Jauncey, D. L., Preston, R. A., et al. 1995, Nature, 374, 141
Turner, M. J. L., Abbey, A., Arnaud, M., et al. 2001, A&A, 365, L27
Ubertini, P., Lebrun, F., Di Cocco, G., et al. 2003, A&A, 411, L131
Ueda, Y., Inoue, H., Tanaka, Y., et al. 1998, ApJ, 492, 782
Ueda, Y., Asai, K., Yamaoka, K., Dotani, T., & Inoue, H. 2001, ApJ, 556, L87
Van der Hooft, F., Heemskerk, M. H. M., Alberts, F., & van Paradijs, J. 1998, A&A, 329, 538
Vedrenne, G., Roques, J.-P., Schönfelder, V., et al. 2003, A&A, 411, L63
Wilms, J., Allen, A., & McCray, R. 2000, ApJ, 542, 914
Winkler, C., Courvoisier, T. J.-L., Di Cocco, G., et al. 2003, A&A, 411, L1
Yamaoka, K., Ueda, Y., Inoue, H., et al. 2001, PASJ, 53, 179
Zhang, S. N., Wilson, C. A., Harmon, B. A., et al. 1994, IAU Circ., 6046, 1